Advanced Steel Construction – Vol. 21 No. 4 (2025) 294–303
DOI:10.18057/IJASC.2025.21.4.2

INVESTIGATION ON THE SEISMIC BEHAVIOR OF END-PLATE CONNECTION BETWEEN STEEL BEAM AND CIRCULAR CONCRETE-FILLED STEEL TUBULAR COLUMN

Shao-Feng Nie [1, *], Zi-Teng Zhao [1], Si-Yuan Chen [1], Yong-Zhen Lin [1], Geng Qin [1] and Xiao-Hui Dong [2]

[1] *School of Civil Engineering, Chang'an University, Shaanxi, China*
[2] *China Railway 16th Bureau Group Corporation Limited, Beijing, China*
** (Corresponding author: E-mail: niesf@chd.edu.cn)*

ABSTRACT

The application and promotion of concrete-filled steel tube (CFST) columns and H-shaped steel beam joints have been extensive in structural engineering. To mitigate stress concentration on columns and protect the panel zone from damage, a fabricated assembly joint was proposed and investigated. This joint comprises a precast concrete-filled steel tube (CFST) column connected to an H-shaped steel beam via an end-plate connection. The joint is assembled conveniently using high-strength bolts, outer diaphragm, and end-plate. Numerical simulation was employed to investigate the seismic behavior of this novel CFST column and H-shaped steel beam joints. Detailed analysis was conducted on failure modes, moment-rotation hysteretic curves, and skeleton curves of specimens subjected to cyclic loading. The results demonstrated that the joint exhibited a full hysteretic curve with excellent seismic performance. Subsequently, a parametric study was conducted to explore a wide range of designs. The results revealed negligible pinch effects in the hysteretic curves and demonstrated excellent joint energy dissipation capacity. All specimens exhibited ductility greater than 3.5. Increasing the thickness of beam end-plate from 12mm to 22mm resulted in a 23.59% increase in initial stiffness but led to a decrease of 13.78% in ductility. Connector end-plates with less than 16mm thickness experienced high stress levels. The position of outer diaphragm significantly influenced the joint's failure mode. Increasing the axial compression ratio from 0.3 to 0.8 reduced the joint's ductility coefficient by 5.2%, suggesting that the axial compression ratio of column limit of 0.7 is recommended for design purposes. Furthermore, increasing the linear stiffness ratio of beam-to-column from 0.18 to 0.59 resulted in a substantial increase in the maximum moment (108.78%) and initial stiffness (90.3%) within specimens. Finally, the reasonable ranges for the thickness of end-plate, the position of outer diaphragm, the axial compression ratio of column, and the linear stiffness ratio of beam-to-column are proposed in this study.

ARTICLE HISTORY

Received: 12 November 2024
Revised: 7 January 2025
Accepted: 8 January 2025

KEYWORDS

End-plate connection;
Concrete-filled steel tubular;
Seismic behavior;
Numerical analysis;
Failure mode;
Design method

1. Introduction

Concrete-filled steel tube (CFST) columns have gained increasing popularity in structural engineering due to their advantageous properties of high ductility and compressive strength. However, the conventional joint connection method for CFST columns to steel beams poses several challenges, including reduced production efficiency and difficulties ensuring construction quality. Therefore, it is crucial to investigate a rational prefabricated joint configuration for the application and advancement of CFST structures.

Based on the recommended code and specification for CFST column-beam joints, various connection forms of CFST column-steel beam composite joints have been proposed. Deng [1] introduced a novel joint design connecting the CFST column and H-shaped beam by welding a vertical diaphragm to the column, thereby enhancing the seismic performance of the panel zone. The study investigated various aspects of the joint's seismic behavior, including failure modes, hysteretic curves, skeleton curves, and ductility. Behrooz [2] proposed a joint connection between a square steel tube column and a steel beam using a connector and an end-plate. Both experimental and numerical analyses have shown that this joint exhibits a full hysteretic curve. Ansari [3] conducted a numerical investigation on stiffener steel beams connected to circular concrete-filled steel tube columns under cyclic loading to explore the effects of different parameters on connection failure modes. Mou [4] proposed a self-centering CFST column-to-H-shaped beam joint that exhibited increased bending capacity with higher axial compression ratios and width-thickness ratios of the steel tube. Tjahjanto [5] investigated the behavior of square CFST columns with direct-welded connections, revealing shear fracture in the column tube plates caused by high-stress concentration at the beam flange and limited joint capacity. Tao et al. [6] conducted an experimental and numerical analysis study on the seismic behavior of composite joints comprising CFST columns, steel beams, and through-bolt connections. The results demonstrated a significant improvement in initial stiffness and ductility. Nie [7-9] performed experimental and numerical investigations on the seismic behavior of steel and composite beam-to-column joints. The findings from both experiments and simulations indicated favorable seismic performance and bearing capacity for these joints.

In the end-plate connection of the composite column, the current research trend is to directly weld the end-plate onto the concrete-filled steel tube and connect the steel beam with high-strength bolts. Experimental research conducted by Wang et al. [10-11] investigated end-plate connections between concrete-filled steel tubular columns and steel beams. The results demonstrated that these single-sided bolted joints were semi-rigid, exhibiting satisfactory ductility according to both American code [12] and Chinese code [13]. Liu et al. [14] presented a numerical study on moment-rotational characteristics of joints between steel beams and circular tubular columns using reverse channels, revealing that all such joints possessed sufficient strength and stiffness to be classified as semi-rigid. Málaga [15] performed an experimental study on beam-to-tubular column connections utilizing combined channel components, examining their stiffness, strength, and energy dissipation properties. Lopes [16] conducted an experimental investigation into the fire resistance of a frame with a U-shaped connection, finding that this type of connection exhibited superior ductility. Nie [17-18] proposed an end-plate connection between an H-shaped steel beam and weak axis of an H-shaped column using a U-shaped connector; results indicated that placing the U-shaped connector in the weak axis formed a box-shaped panel zone with increased volume within which shear deformation resistance was enhanced.

There is limited research available on fabricated circular steel tube concrete-steel beam joints in current literature. Existing connection methods for circular steel tube concrete columns and beams primarily focus on outer diaphragm connections, welded connections, and end-plate connections. The single connection method exhibits several significant drawbacks. Specifically, the welding connection incurs considerable construction costs, and the seismic and energy dissipation performance of end-plate connected joints requires further improvement. Additionally, the connection between H-shaped steel beams and circular steel tubular columns presents challenges due to the non-uniform outer surface. This paper innovatively integrates outer diaphragm and end-plate connections to address these issues.

The novel joint, which integrates the outer diaphragm, end plate, and stiffener, demonstrates significantly improved seismic behavior. These components effectively mitigate stress concentration on columns, thereby protecting the panel zone from damage. A finite element model (FEM) was developed using Abaqus to analyze the novel joint. The comprehensive analysis included discussions on failure modes, hysteresis curves, skeleton curves, bearing capacity and ductility. Furthermore, parametric investigations were conducted to assess the impact of parameters such as beam end-plate, connector end-plate, position of the outer diaphragm, axial compression ratio and linear stiffness ratio of the beam-to-column on bearing capacity. Based on these analytical results, design recommendations were proposed for CFST structures. The joint is illustrated in Fig. 1.

2. Design of specimen

The basic specimen was designed following the 'Technical Code for Steel Structure of Light-weight Building with Gabled Frames' (GB 51022-2015) [19]. M22 high-strength bolts of grade 10.9 were used to connect the column and beam, while concrete with a strength grade of C40 was utilized in all specimens. The steel used was documented in Q235. The preloading force of the bolt was 190 kN. The configuration and dimension of the basic specimen are illustrated in Fig. 2.

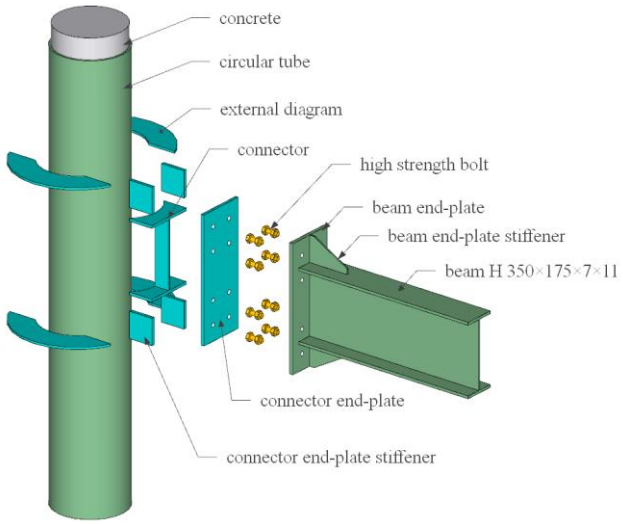

Fig. 1 Connection of the basic specimen configurations

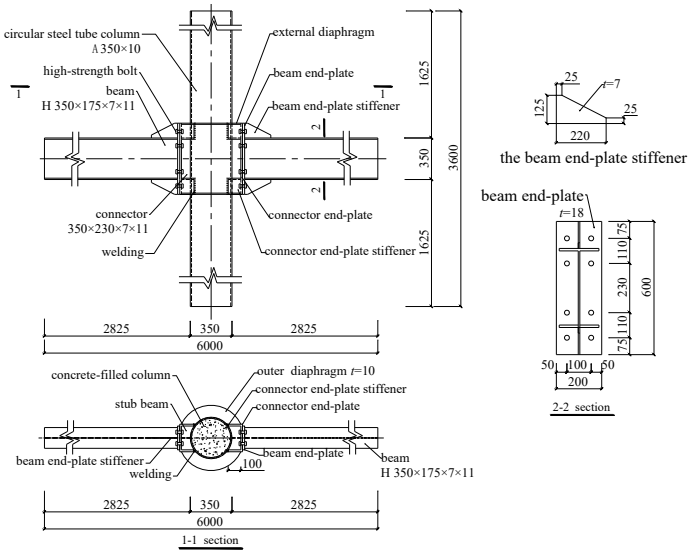

Fig. 2 Detail of the BASIC specimen (unit: mm)

3. Establishment and verification of finite element model

3.1. Constitutive relationship setting and element selection

A double-broken line model was employed to simulate the stress-strain relationships of steel and high-strength bolts. The elastic modulus of steel was 206,000 MPa, with a Poisson's ratio of 0.3. The yielding strength, ultimate strength, and ultimate strain of the steel were determined as 235 MPa, 420 MPa, and 0.15 respectively. For the high-strength bolts, the yielding strength, ultimate strength and ultimate strain were found to be 940 MPa, 1130 MPa, and 0.10 respectively.

Solid elements (C3D8R) were utilized throughout the finite element model FEM analysis for all components involved in this study.

3.2. Boundary conditions and interactions

The loading scheme is shown in Fig. 3. The boundary conditions were designed to accurately replicate real-world scenarios. Incorrect boundary conditions could result in erroneous outcomes. For the BASIC specimen, reference points RP1 and RP5 were established at the top and bottom of the column, respectively. All degrees of freedom at the top and bottom surfaces of the column were coupled with RP1 and RP5, respectively. Additionally, the degrees of freedom on the side flange surface of the top column with a length of 50 mm were coupled with RP2. Displacement constraints were applied to prevent lateral displacement instability during loading by restricting movement within 50 mm from the loading point on the side surface of the beam flange.

'Tie' contact was implemented for welding positions. According to the "Steel Structure Design Standard" (GB 50017-2017) [20], the tangential friction coefficient between the contact surfaces of the beam, end-plate, and high-strength bolts was specified as 0.4. For the interface between the steel tube and infilled concrete, a frictional contact model with a tangential friction coefficient of 0.2 [21] was employed, while hard contact behavior was used in the normal direction to accurately simulate realistic contact conditions.

To ensure that no instability occurred when the axial compression and the displacement were applied to the column. X, Y direction displacement constraints and X, Z direction rotational constraints were applied to RP1. Y, Z direction displacement constraints and X, Z direction rotational constraints were applied to RP3 and RP4. X, Y, Z direction displacement constraints and X, Z rotational constraints were applied to RP5. The boundary conditions and mesh division are depicted in Fig. 4.

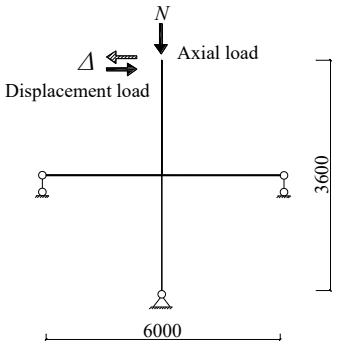

Fig. 3 Loading scheme (unit: mm)

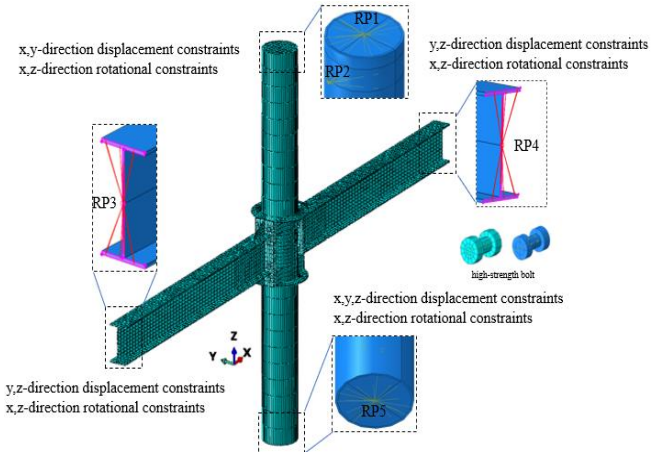

Fig. 4 Boundary Conditions and grid division of the BASIC specimen

3.3. Loading process

The loading process is illustrated in Fig. 5. Initially, a constant axial compression load was applied at the top of the column which remained throughout the entire loading process followed by low cyclic loading applied to RP2 as per American seismic provision ANSI/AISC341-10 [22]. The loading control was based on inter-story drift angle criteria until reaching an ultimate value corresponding to an inter-story drift angle equaling 0.06 rad.

3.4. Verification of FEM

To validate the feasibility and accuracy of the FEM analysis method adopted herein, the first SB-4E model based on reference [23] was established using the aforementioned approach. Secondly, FEM results obtained through

analysis were compared against experimental findings to verify correctness. The experimental setup, loading scheme and detailed information of the SB-4E specimen are illustrated in Figs. 6, 7 and 8. The material properties are presented in Table 1. The cyclic loading point for specimen SB-4E is located at the beam end, and the loading process, as detailed in reference [23], is identical to that applied to the specimens shown in Fig. 5.

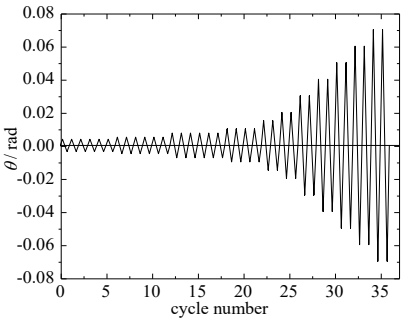

Fig. 5 Loading process

Fig. 6 Experimental setup and specimen

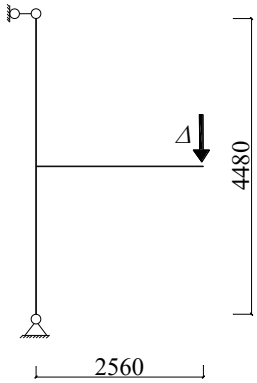

Fig. 7 Loading scheme of the SB-4E specimen

The failure modes, moment-rotation hysteretic curves, and skeleton curves obtained from both FEM analysis and experiments are presented in Figs. 9 and 10. A comparison between the FEM analysis and test results is provided in Table 2. The inter-story drift angle θ and beam moment M are calculated using Eqs (1) and (2), respectively [24-25].

$$\theta = \arctan\frac{\Delta}{H} \tag{1}$$

$$M = R_1 l \tag{2}$$

Where Δ represents the horizontal displacement; H represents the height from the loading point to the bottom of the column; R_1 represents the reaction force of the end of the left beam; l represents the distance from the beam end to the surface of the connector; M_p represents the plastic moment of the whole section of the beam.

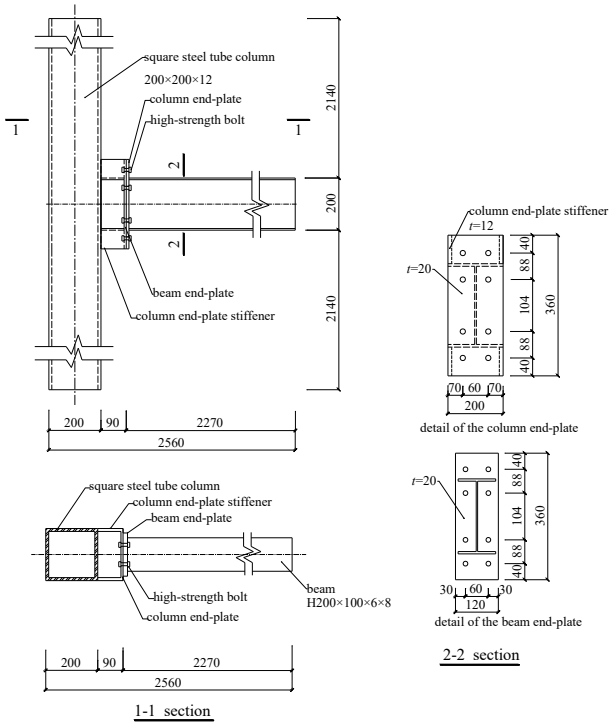

Fig. 8 Details of the SB-4E specimen (unit: mm)

Table 1
Material properties of SB-4E

Element	Thickness or Diameter / mm	Yield stress / MPa	Ultimate strength / MPa
Beam flange & stiffener	8	327.0	480.2
Beam web & stiffener	6	307.0	410.0
Beam end-plate	20	262.8	428.0
Column end-plate	12	270.5	459.7
High-strength bolt	16	925.0	1147.8

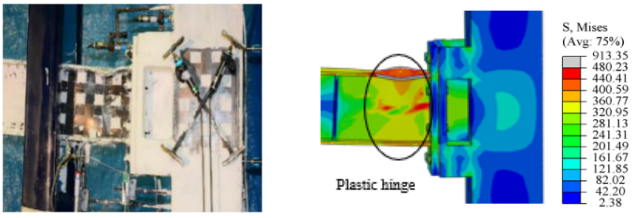

(a) Failure mode of the test result (b) Failure mode of the FEM result

Fig. 9 Comparison of failure mode

Figs. 9 and 10 demonstrated that the skeleton curves obtained from FEM analysis align well with those obtained from experiments. During the experiment, significant deformation occurred on the beam flange. In the FEM analysis, high-stress regions were concentrated near the beam flange and web where stress values reached their ultimate limits.

Table 2 revealed that there was less than a 5% difference between M_y and M_{max} as determined by FEM analysis compared to experimental results. The

FEM analysis demonstrated that the failure mode and hysteresis curve obtained from the simulation align well with the experimental results, indicating the validity and reliability of the FEM model for subsequent analyses.

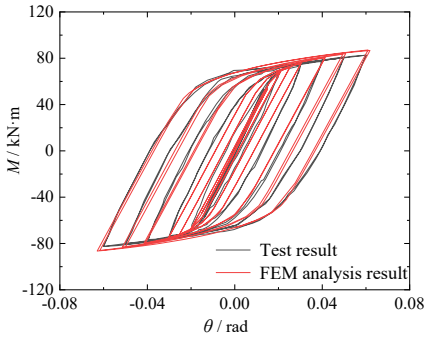

(a) Hysteretic curves

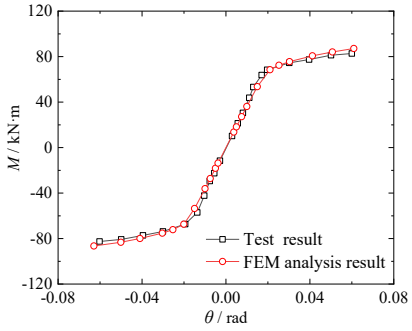

(b) Skeleton curve

Fig. 10 Comparison of hysteretic curves, and skeleton curves

Table 2
Comparison of FEM analysis and test results

Loading direction	M_y / kN·m			M_{max} / kN·m		
	Test	FEM	comparison	Test	FEM	comparison
+	69.4	71.1	2.39%	82.7	86.8	4.72%
−	67.9	70.7	3.96%	82.6	86.5	4.51%

Note: M_y and M_{max} represent the yielding moment and the maximum moment of the joint, respectively.

4. Seismic behavior of BASIC specimen

To investigate the seismic behavior of specimen BASIC, we analyzed its failure mode, hysteretic curve, skeleton curve, and ductility using FEM analysis. In this study's approach to damage assessment during the testing phase within elastic range was defined as load dropping to below 85% of maximum load value.

4.1. Moment-rotation hysteretic curve and skeleton curve

A mesh-sensitivity analysis was performed in the numerical simulations for joints to examine the influence of varying mesh sizes on the mechanical behavior of the specimens. The mesh-sensitivity analysis is illustrated in Fig. 11. Considering both the accuracy of the results and the computational cost, a 40 mm × 40 mm grid was selected for the panel zone, while a 100 mm × 100 mm grid was chosen for the beam, column, and concrete elements. Fig. 11 illustrates both the moment-rotation hysteretic curve and skeleton curve for specimen BASIC while Table 3 provides corresponding results.

As shown in Fig. 11 and Table 3, the hysteretic curve of the BASIC specimen was full and exhibited no pinching behavior, indicating that strong energy dissipation capacity was possessed by the BASIC specimen. The hysteretic loop area of the specimen BASIC increased continuously with the loading process, indicating that the energy dissipation behavior of the specimen was improved. The ductility coefficient of the BASIC specimen was 3.89, indicating excellent resistance to deformation under cyclic loading conditions.

The FEM analysis results were compared with those of the joint proposed by Brehooz [2]. Both types of joints exhibited an optimal failure mode by positioning the end-plate at the connection, ensuring that the plastic hinge formed well outside the panel zone. The presence of the outer diaphragm in this study effectively protected the end-plate and column, preventing stress concentrations from reaching the yield stress in this critical area.

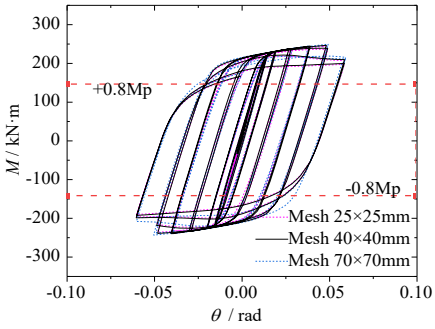

(a) Hysteretic curve

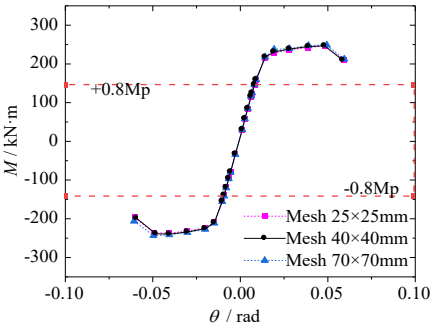

(b) Skeleton curve

Fig. 11 Hysteresis and skeleton curves of the BASIC specimen under varying mesh sizes

Table 3
FEM analysis results of the BASIC specimen

Mesh size	M_y /kN·m	θ_y /rad	M_{max} /kN·m	θ_{max} /rad	M_u /kN·m	θ_u /rad	μ
40×40mm	215.8	0.02	244.1	0.05	207.5	0.06	3.89
25×25mm	215.6	0.02	243.9	0.05	207.3	0.06	3.87
70×70mm	216.4	0.02	246.9	0.05	209.8	0.06	3.86

Note: M_u represents the failure moment of the joint. θ_y, θ_{max} and θ_u represent the inter-story drift angles at the yielding moment, maximum moment, and failure moment, respectively. μ represents the rotational ductility coefficient, calculated as $\mu=\theta_u/\theta_y$

4.2. Failure mode and failure process

Fig. 12 illustrates the failure mode and Von Mises stress distribution of the BASIC specimen.

It can be observed from Fig. 12 that plastic hinges formed at the beam when the joint was damaged. The outer diaphragm effectively protected the connection region between the connector and circular steel tube column, while minimal damage occurred in the panel zone, end-plate and high-strength bolts.

5. Parametric study

The study further investigated various parameters including the thicknesses of beam end-plate and the connector end-plate, the position of outer diaphragm, the axial compression ratio of the column, and the linear stiffness ratio of beam-to-column. The detailed parameters and results of specimens is shown in Table 4

5.1. The thickness of beam end-plate

Three specimens were established for the A series with different thicknesses: A-1 (0.55 d_0), A-2 (0.73 d_0), and A-3 (1.00 d_0) where d_0 represents the M22 bolt diameter. Contours depicting Von Mises stress distribution under failure modes for A series specimens are presented in Fig 13 while hysteretic curves and skeleton curves are shown in Figs. 14 and 15 respectively.

As shown in Fig. 13, The failure modes of specimens BASIC and A-3 exhibited similarities to the BASIC specimen, with plastic deformation

occurring at both the beam flange and web, far away from the joint. The stress experienced by the beam end-plate was relatively low. In contrast, for specimen A-1, under the applied failure load, significant deformation was observed in the beam end-plate, accompanied by a concentration of stress at the weld between the beam flange and end-plate.

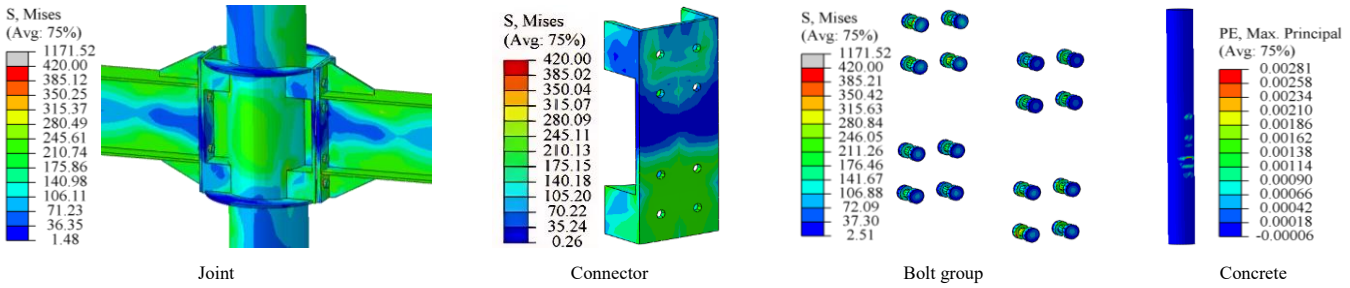

(a) Von Mises stress and strain at yielding load

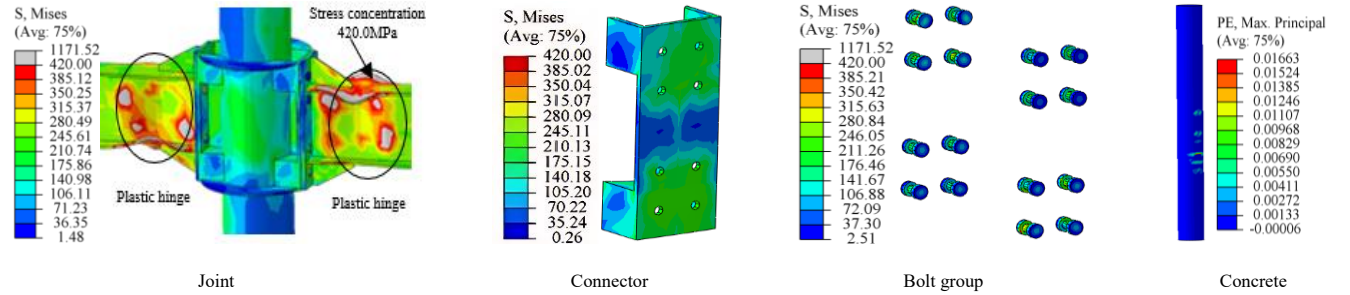

(b) Von Mises stress and strain at failure load

Fig. 12 Contour of the Von Mises stress and strain of BASIC specimen

Table 4
The parameters and results of specimens

Specimen	t_1 / mm	t_2 / mm	d	n	k	M_y / kN·m	θ_y / rad	M_{max} / kN·m	θ_{max} / rad	M_u / kN·m	θ_u / rad	μ
A-1	12	14	1.00	0.3	0.33	176.0	0.017	235.1	0.060	235.1	0.080	4.71
A-2	16	14	1.00	0.3	0.33	211.1	0.015	243.9	0.050	207.3	0.059	3.90
BASIC	18	14	1.00	0.3	0.33	215.8	0.015	244.1	0.050	207.5	0.059	3.89
A-3	22	14	1.00	0.3	0.33	213.7	0.015	244.7	0.050	208.0	0.057	3.88
B-1	18	10	1.00	0.3	0.33	183.2	0.016	243.6	0.060	207.1	0.069	4.29
B-2	18	16	1.00	0.3	0.33	216.2	0.015	244.3	0.050	207.6	0.059	4.02
B-3	18	20	1.00	0.3	0.33	217.5	0.014	244.7	0.050	208.0	0.058	4.10
C-1	18	14	0	0.3	0.33	214.3	0.015	243.2	0.050	206.7	0.059	3.84
C-2	18	14	0.50	0.3	0.33	214.9	0.015	243.4	0.050	206.9	0.059	3.86
C-3	18	14	1.00	0.3	0.33	215.8	0.015	244.11	0.05	207.49	0.059	3.88
D-1	18	14	1.00	0.4	0.33	214.4	0.015	244.1	0.050	207.4	0.059	3.88
D-2	18	14	1.00	0.5	0.33	213.0	0.015	244.0	0.050	207.4	0.059	3.82
D-3	18	14	1.00	0.6	0.33	211.9	0.015	243.9	0.040	207.3	0.059	3.78
D-4	18	14	1.00	0.7	0.33	210.8	0.015	243.7	0.040	207.2	0.059	3.76
D-5	18	14	1.00	0.8	0.33	208.5	0.015	243.2	0.040	206.8	0.059	3.68
E-1	18	14	1.00	0.3	0.18	143.1	0.015	168.0	0.050	142.8	0.068	4.59
E-2	18	14	1.00	0.3	0.46	267.8	0.015	320.4	0.050	272.4	0.059	3.87
E-3	18	14	1.00	0.3	0.59	301.9	0.018	350.8	0.050	304.6	0.059	3.39

Note: t_1 represents the thickness of beam end-plate; t_2 represents the thickness of connector end-plate; d represents the ratio of the vertical distance of the outer diaphragm to the height of the connector end-plate; n represents the axial compression ratio; k represents the linear stiffness ratio of the beam-to-column.

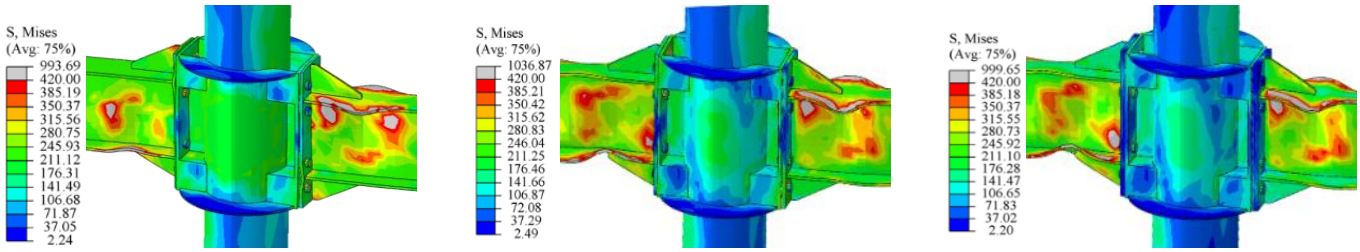

(a) A-1 (b) A-2 (c) A-3

Fig. 13 The contour of the Von Mises stress of A series specimens under failure modes

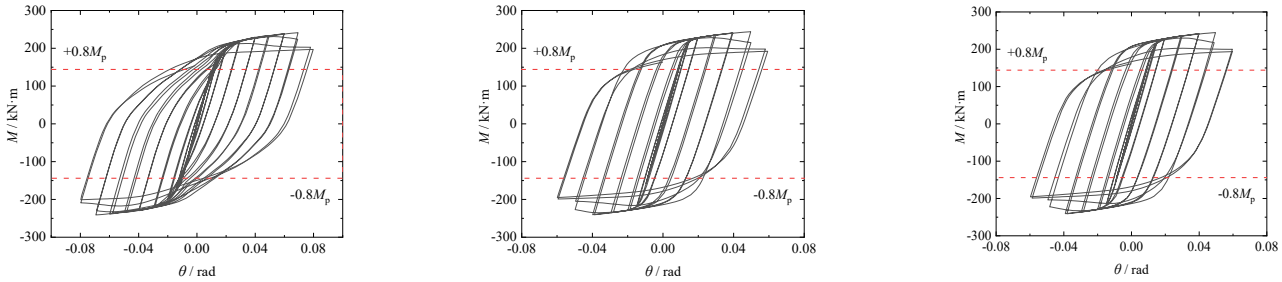

(a) A-1 (b) A-2 (c) A-3

Fig. 14 Hysteretic curves of A series specimen

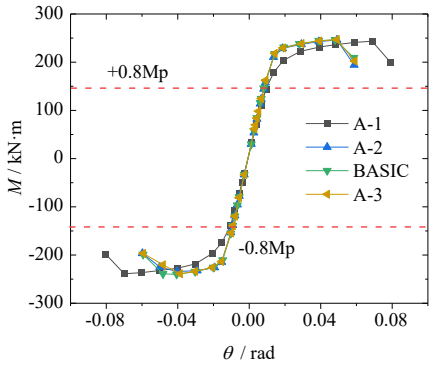

Fig. 15 Skeleton curves of A series specimen

As shown in Figs. 14 and 15, all specimens within the A series exhibited full hysteretic curves during loading cycles with similar initial-stage skeleton curves. However, the maximum moment slightly increased as a function of increasing beam end-plate thickness. Specifically, varying beam end-plate thickness from 12 to 22mm resulted in a maximum moment increase of approximately 4.1% accompanied by a reduction in ductility coefficient by 23.5%. Despite this decrease in ductility coefficient values among all joints remained above 3.6, indicating satisfactory ductile behavior. The influence of the beam end-plate thickness on both the ductility and failure mode of the joint was found to be significant, while its effect on bearing capacity was comparatively minor.

To ensure a reasonable formation of the plastic hinge within an acceptable range of deformation for the beam end-plate, it is recommended that the thickness t_1 should exceed 16mm (0.73 d_0).

5.2. The thickness of connector end-plate

The thickness of connector end-plate was varied with values of 10mm (0.45d_0), 16mm (0.73d_0), and 20mm (0.91d_0). B-1, B-2 and B-3 specimens were established correspondingly. Von Mises stress of B series specimens under failure mode was shown in Fig. 16, hysteresis curves and skeleton curves were shown in Figs. 17 and 18, respectively.

As shown in Fig. 16, the B-1 specimen failed to form an obvious plastic hinge on the beam. The deformation of the joint was primarily concentrated at the connector end-plate due to its thinner thickness. Once the thickness of the connector end-plate exceeded 14mm, a consistent failure mode was observed across all specimens. Plastic hinges formed away from the panel zone in the beam while maintaining an elastic state without significant deformation in the panel zone itself. Moreover, when surpassing a thickness of 16mm, the end-plate effectively protected both the column and panel zone, facilitating plastic hinge formation in the beam. Varying connector end-plate thickness from 10 to 20mm resulted in a mere increase of 0.45% maximum moment and a reduction of ductility coefficient by 4.6% for specimens."

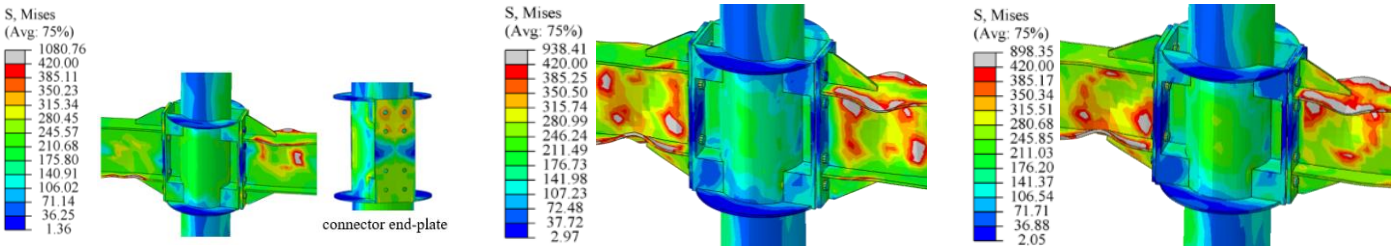

(a) B-1 (b) B-2 (c) B-3

Fig. 16 The contour of the Von Mises stress of B series specimens under failure modes

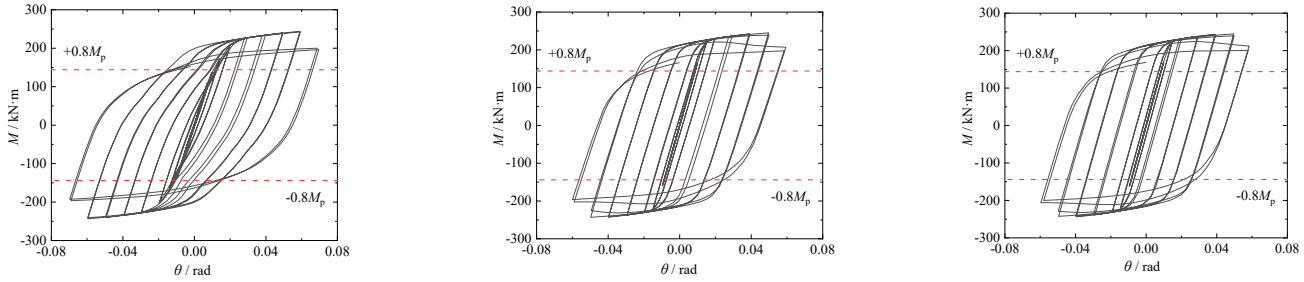

(a) B-1 (b) B-2 (c) B-3

Fig. 17 Hysteretic curves of B series specimens

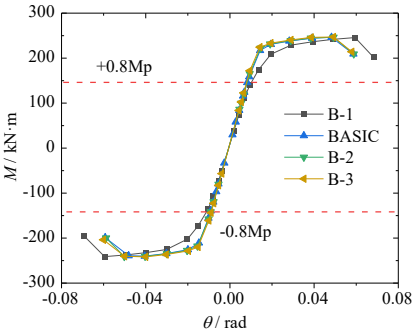

Fig. 18 Skeleton curves of B series specimens

As depicted in Figs. 17 and 18, specimen B-1 exhibited incomplete hysteretic loops due to the reduced thickness of the connector end-plate. This deficiency led to significant deformation of the end-plate during loading, insufficient development of plastic hinges at the beam, and suboptimal energy dissipation behavior of the specimens. However, when the thickness of the connector end-plate exceeded 12mm ($0.55d_0$), all specimens demonstrated complete hysteretic loops. Moreover, across all specimens, skeleton curves indicated that a connector end-plate thickness exceeding 14mm weakened its influence on seismic behavior, thereby satisfying seismic requirements [19].

5.3. The position of outer diaphragm

The position of outer diaphragm represents the ratio of the vertical distance of the outer diaphragm to the height of the connector end-plate. Three different positions of outer diaphragm were considered, namely 0, 0.50, and 1.00. Consequently, C-1, C-2, and C-3 specimens were established correspondingly. Fig. 19 illustrates the contours of Von Mises stress for E series specimens under various failure modes, while Figs. 20 and 21 present hysteretic and skeleton curves respectively.

As shown in Fig. 19, If the outer diaphragm position of the specimen is less than 0.50, the connector end-plate would also yield when the joint was damaged. If the outer diaphragm position of the specimen was 0.50, the failure mode of the joint was similar to that of the basic specimen. When the plastic deformation was formed at the beam, there was no obvious deformation in the panel zone.

Figs. 20 and 21 indicated that C-2 and C-3 exhibit superior energy dissipation capacity compared to other specimens, suggesting that the elevated position of the outer diaphragm effectively safeguards the column and panel zone. This configuration ensured predominantly elastic behavior with minimal deformation in both the panel zone and column. Furthermore, as the position of the outer diaphragm ascended from the beam flange towards the upper end-plate connector, there was a slight increase in maximum load and ductility for this specimen. It was recommended that a minimum outer diaphragm position greater than 0.5 be adopted to ensure an optimal failure mode for specimens.

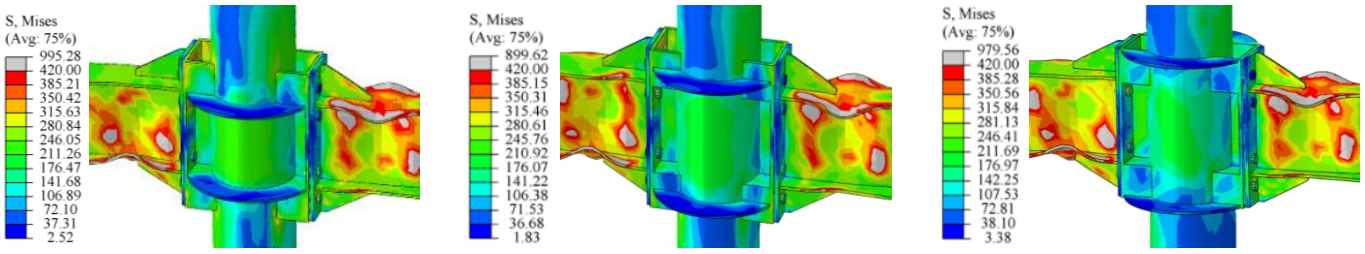

(a) C-1 (b) C-2 (c) C-3

Fig. 19 The contour of the Von Mises stress of C series specimens under failure modes

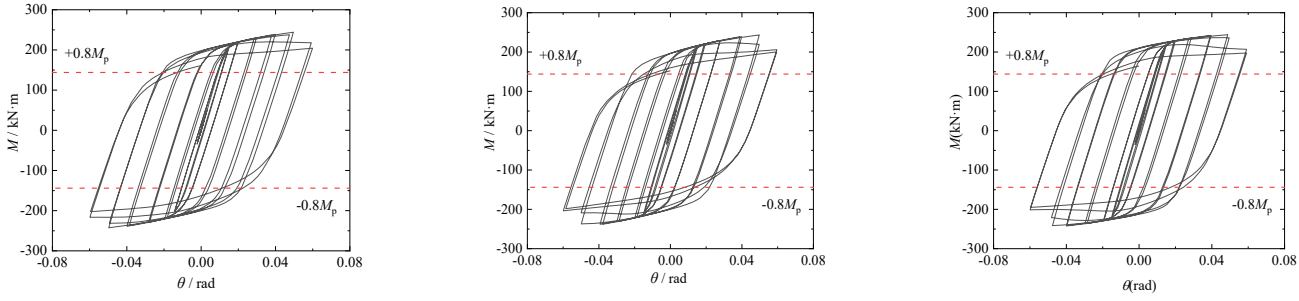

(a) C-1 (b) C-2 (c) C-3 (BASIC)

Fig. 20 Hysteretic curves of E series specimens

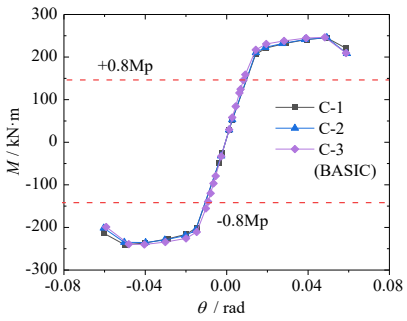

Fig. 21 Skeleton curves of E series specimens

*5.4. The axi*al compression ratio of column

The axial compression ratio of the column was determined following the Chinese code [26]. The axial compression ratio '*n*' for the concrete-filled steel tubular column is calculated using Eq (3).

$$n = \frac{N}{f_c A_c + f_s A_s} \tag{3}$$

Where N represents the design value of the concentrated load; f_c and f_s represent the design compressive strength of concrete within the column and the design compressive strength of steel, respectively; A_c and A_s represent the concrete cross-sectional area and steel pipe cross-sectional area, respectively.

The axial compression ratio of the column was varied, with values ranging from 0.4 to 0.8. Specimens D-1, D-2, D-3, D-4, and D-5 were established correspondingly.

Fig. 22 illustrates the contours of Von Mises stress for the failure modes observed in the series of specimens labeled as "D". Additionally, Figs. 23, 24 and 25 present the hysteretic and skeleton curves respectively.

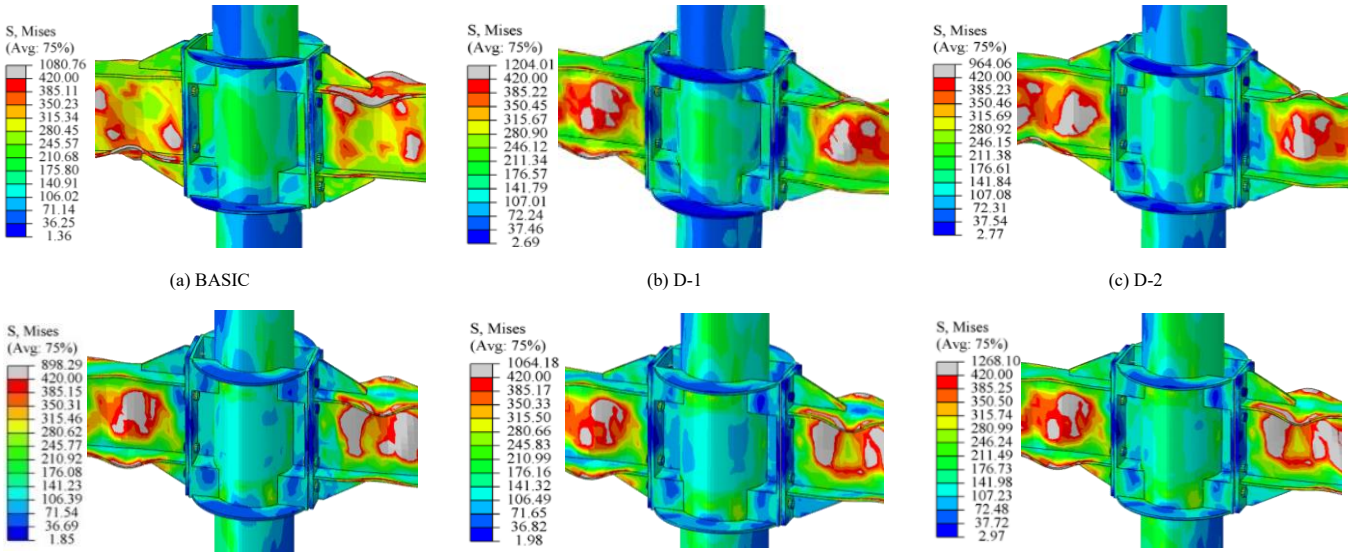

(a) BASIC (b) D-1 (c) D-2

(d) D-3 (e) D-4 (f) D-5

Fig. 22 The contour of the Von Mises stress of D series specimens under failure modes

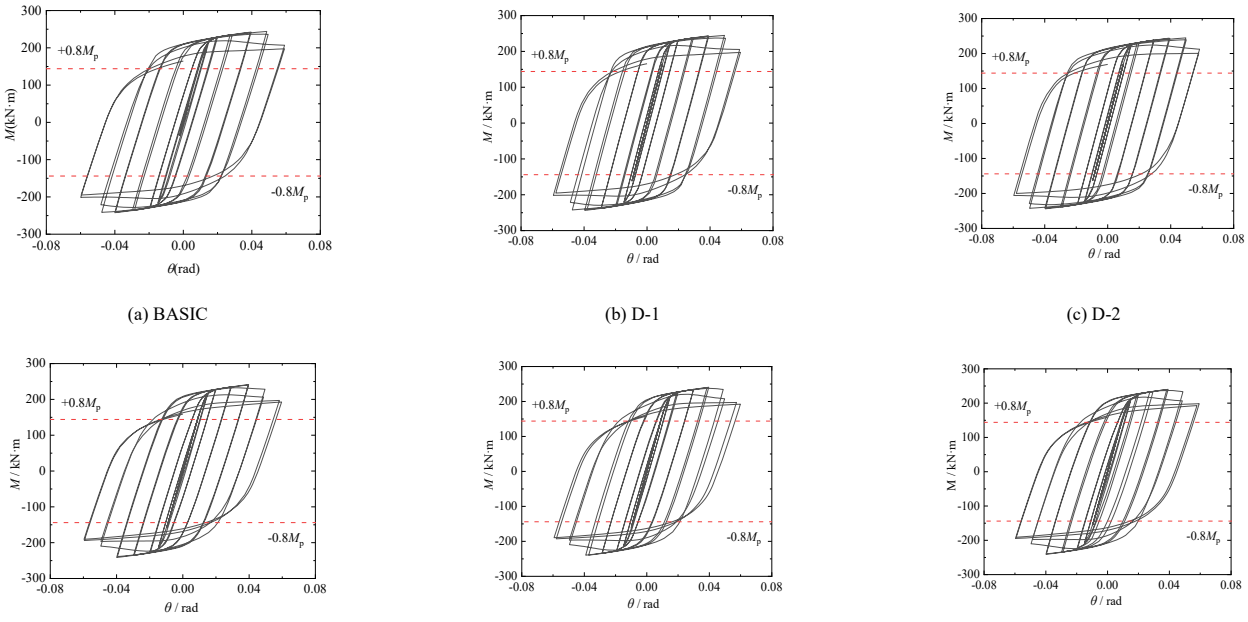

(a) BASIC (b) D-1 (c) D-2

(d) D-3 (e) D-4 (f) D-5

Fig. 23 Hysteretic curves of D series specimens

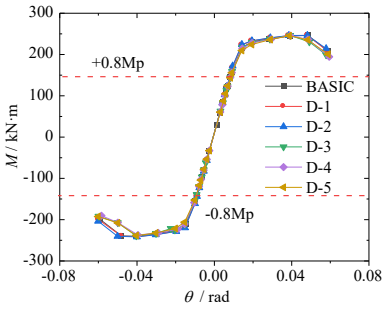

(a) *M-θ* skeleton curves

Fig. 24 *M-θ* Skeleton curves of D series specimens

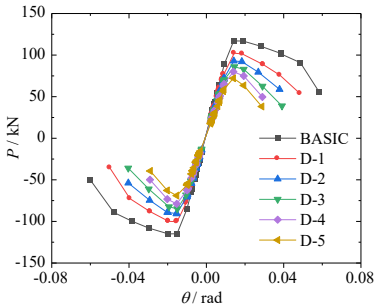

(b) *P-Δ* skeleton curves

Fig. 25 *P-Δ* Skeleton curves of D series specimens

As depicted in Fig. 22, an increase in the axial compression ratio from 0.3 to 0.8 resulted in the formation of plastic hinges at the beam of each D specimen, and similar failure modes were observed for all D specimen joints, indicating that the axial compression of the column had minimal influence on the failure mode.

The *M-θ* hysteretic curves of each specimen in the D series exhibited the same shape, as depicted in Figs. 23 and 24. During the initial loading phase, there was minimal variation in the initial stiffness of the skeleton curve among specimens. Furthermore, an increase in the axial compression ratio resulted in reductions in both the initial and peak loads of specimens, accompanied by an accelerated load reduction rate. As shown in Fig. 25, the *P-Δ* skeleton curves revealed that with increasing axial compression ratio, there were significant decreases observed in the initial stiffness, maximum load, and decline rate of bearing capacity for each specimen. This phenomenon indicated an enhanced second-order effect due to an increased axial compression ratio.

As the axial compression ratio continued to rise, a gradual decrease was observed in ductility for all specimens examined. Specifically, when increasing from 0.3 to 0.8, there was only a marginal reduction from 3.88 to 3.81 observed for rotational deformation's ductility coefficient—a relatively minor decrease overall. It is recommended that designers maintain the axial compression ratio below 0.7 to ensure satisfactory ductility behavior within specimens.

5.5. The linear stiffness ratio of beam-to-column

The linear stiffness ratio of beam-to-column '*k*' is calculated by Eq (4).

$$k = \frac{E_b I_b / l_c}{E_c I_c / l_b} \tag{4}$$

Where E_bI_b and E_cI_c represented the elastic flexural rigidity of beams and columns respectively. l_c represented the vertical distance between the upper and lower support centers of the column, and l_b represented the horizontal distance of the beam.

The section sizes of the beams were modified to H300 × 150 × 6.5 × 9, H350 × 175 × 7 × 11, H450 × 150 × 8 ×13, and H400×200×8×13 for E-1, E-2, and E-3 specimens with linear stiffness ratios varying between 0.18 to 0.59 relative to the column. Fig.26 illustrates the Von Mises stress of the H series specimens under failure modes while Figs.27 and 28 depict their hysteretic and skeleton curves.

As depicted in Figs. 26 and 27, for linear stiffness ratios of 0.18, 0.33, and 0.46 between the beam and column, these specimens exhibited significant plastic deformation of the beam flange upon reaching failure load, while maintaining low stress levels in the panel zone and column. However, when the beam-column stiffness ratio was increased to 0.59, local plastic deformation occurred at the connector end-plate during specimen damage. The plastic hinge of the beam was located near the beam end-plate but not fully developed. Consequently, with a linear stiffness ratio of 0.59, the joint design failed to meet seismic design requirements.

The maximum moment increased by 108.8% as depicted in Fig. 28, while the ductility coefficient of specimens decreased by 33.1% when varying the linear stiffness ratio of the beam-to-column from 0.18 to 0.59. The maximum moment of the beam is significantly influenced by the linear stiffness ratio of the beam-to-column, which exhibits a negative correlation with its ductility behavior.

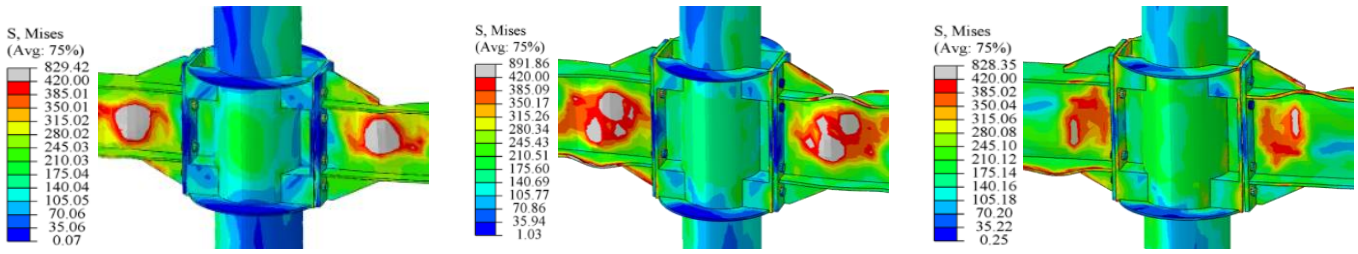

(a) E-1 (b) E-2 (c) E-3

Fig. 26 The contour of the Von Mises stress of E series specimens under failure modes

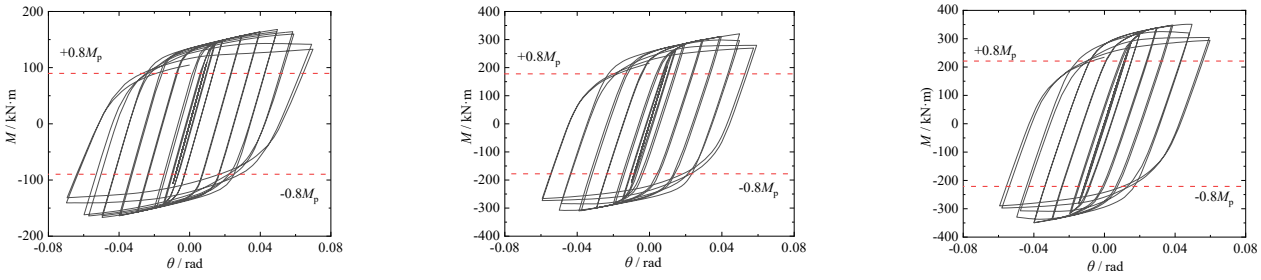

(a) E-1 (b) E-2 (c) E-3

Fig. 27 Hysteretic curves of E series specimens

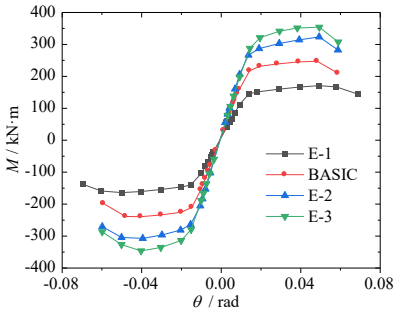

Fig. 28 Skeleton curves of E series specimen

The ideal failure mode of the specimen occurred when the linear stiffness ratio of the beam-to-column was below 0.59. To ensure a joint with strong bearing capacity and an optimal failure mode, it is recommended to limit the linear stiffness ratio of beam-to-column between 0.35 and 0.55.

6. Conclusions

Based on the finite element analysis of the seismic behavior exhibited by the BASIC specimen, a comprehensive investigation is conducted to further scrutinize the intricate effects of various parameters. Consequently, meticulous examination of these outcomes leads to the formulation of the subsequent conclusions.

(1) The end-plate connection between a steel beam and a circular CFST column exhibits excellent rotation and deformation capacity, making it a semi-rigid joint. By incorporating stiffeners and an outer diaphragm in the panel zone, the plastic hinge can be effectively relocated away from the panel zone, thereby preventing stress concentration on the end-plate. The failure mode of the BASIC specimen satisfies the principle of 'strong joints and weak members'.

(2) The seismic behavior of the joint is influenced by the thickness of the beam end-plate. Optimal end-plate thickness not only maximizes the load-bearing capacity of bolts and end-plates but also ensures superior joint ductility. The position of outer diaphragm significantly impacts the failure mode of the joint. The ductility of the joint decreases as axial compression ratio increases. When the linear stiffness ratio of beam-to-column is less than 0.59, specimens exhibit high bearing capacity and good ductility.

(3) The proposed parameter values are as follows: the thickness of beam end-plate should exceed 16mm, and the thickness of connector end-plate should be greater than 12mm. The position of outer diaphragm should be above 0.5. The axial compression ratio of the specimen is limited to 0.7. It is recommended that the linear stiffness ratio of beam-to-column falls within a range of 0.35 to 0.55.

(4) The joint proposed in this paper integrates the outer diaphragm with bolts, significantly enhancing construction efficiency and reducing costs. These advantages will be further investigated in subsequent research. The findings presented in this paper provide a theoretical foundation for engineering applications.

Notations

N - The design value of the axial load
Δ - The horizontal displacement
H - The height from the loading point to the bottom of the column
R_1 - The reaction force of the end of the left beam
l - The distance from the beam end to the surface of the connector
M_p - The plastic moment of the whole section of the beam
M_y - The yielding moment of the joint
M_{max} - The maximum moment of the joint
θ_y - The inter-story drift angle under the yielding moment of the joint
θ_{max} - The inter-story drift angle under the maximum moment of the joint
M - The beam moment
θ - The inter-story drift angle
R_{ki} - The initial stiffness
M_u - The failure moment of the joint
θ_u - The inter-story drift angle under the failure moment of the joint
μ - The rotational ductility coefficient
t_1 - The thickness of beam end-plate
t_2 - The thickness of connector end-plate
d - The position of outer diaphragm
n - The axial compression ratio of column
k - The linear stiffness ratio of beam-to-column
A_c - The concrete cross-sectional area.
A_s - The steel pipe cross-sectional area
E_bI_b - The elastic flexural rigidity of the beam
E_cI_c - The elastic flexural rigidity of column
l_c - The vertical distance between the upper and lower support centers of the column.
l_b - the horizontal distance of the beam.

Acknowledgments

The authors sincerely acknowledge the financial support provided by the Key Research and Development Program of Shaanxi (No.2021SF-519, No.2024GX-YBXM-374).

References

[1] Deng F.E., Wu T.S. and Qian H., "Seismic Performance and Design of an Innovative Dual Vertical Diaphragms Joint Between Flat CFST Column and H-Beam", Journal of Building Engineering, 2024, 87: 108945.
[2] Behrooz M.S. and Erfani S., "Parametric Study of Stub-Beam Bolted Extended End-Plate Connection to Box-Columns", Journal of Constructional Steel Research, 2020, 171: 106155.
[3] Ansari M., Jeddi M.Z., Badaruzzaman W.H.W., Tahir M.M., Osman S.A. and Hosseinpour E. "A Numerical Investigation on the Through Rib Stiffener Beam to Concrete-Filled Steel Tube Column Connections Subjected to Cyclic Loading", Engineering Science and Technology, An International Journal, 2020, 24(3): 728-735.
[4] Mou B., Yan X.C., Yu Y.J. and Wang Z.A. "Composite CFST Column to H-shaped Steel Beam Joint: Experimental and Numerical Investigation[J]. Engineering Structures", 2024, 299: 117083
[5] Tjahjanto H., MacRae G. and Abu A., "Behaviour of Improved Direct-Welded Connections in Square CFST Column Moment Frames Under Bidirectional Loading", Advanced steel construction, 2020, 16(02): 156-169.
[6] Tao Z., Li W., Shi B.L. and Han L.H, "Behaviour of Bolted End-Plate Connections to Concrete-Filled Steel Columns", Journal of Constructional Steel Research, 2017, 134: 194-208.
[7] Nie S.F., Zhang B. and Ye M.N., "An Investigation on the Seismic Behavior of Circular Steel Tube Confined SRC Column-RBS Joints with RC Ring Beam", Progress in Steel Building Structures, 2022, 24(09): 1-11. (in Chinese)
[8] Nie S.F., Ye M.N., Wu Y.F., Ding, W.X. and Zhu, J.Z., "Seismic Behavior of Square Tube Confined Steel-Reinforced Concrete Column-RC Ring Beam Joint", Journal of Architecture and Civil Engineering, 2019, 36(02): 84-91. (in Chinese)
[9] Nie S.F., Zhu J.Z. and Ma Y., "Study on Mechanical Behavior of Castellated Beam-Solid Column Cruciform Joints", Journal of Architecture and Civil Engineering, 2018, 35(04): 63-71. (in Chinese)
[10] Wang J.F., Zhang L. and Dai Y, "Seismic Experimental Study of End-Plate Connections for Semi-Rigid Concrete-Filled Steel Tubular Frames". China Civil Engineering Journal, 2012, 45(11): 13-21. (in Chinese)
[11] Wang J.F., Jiang S. and Guo L., "Experimental Study on Seismic Performance of Concrete-Filled Double Steel Tubular Column Composite Connections with High Strength Blind Bolts", Journal of Building Structures. 2021, 42(01): 93-102. (in Chinese)
[12] FEMA-350, Recommended Seismic Design Criteria for New Steel Moment-Frame Buildings, Federal Emergency Management Agency, Washington, American, 2009.
[13] GB 50011-2016, Code for Seismic Design of Buildings, Ministry of Housing and Urban-Rural Development of the People's Republic of China, Beijing, China, 2016. (in Chinese)
[14] Liu H. and Wang Y.C., "A Numerical Study of the Behaviour of Steel Beam to Tubular Column Joints Using Reverse Channel", Progress in Steel Building Structures, 2010, 12(04): 5-10. (in Chinese)
[15] Málaga-Chuquitaype C. and Elghazouli A., "Behaviour of Combined Channel/Angle Connections to Tubular Columns under Monotonic and Cyclic Loading", Engineering Structures, 2010, 32(6): 1600-1616.
[16] Lopes, F. and Santiago, A., "Sub-Frames with Reverse Channel Connections to CFT Composite Columns - Experimental Evaluation", Advanced Steel Construction, 2015, 11(1): 111-125.
[17] Nie S.F., Wang S., Liu B., Liu Z. and Han, Y., "Study on The Seismic Behavior of Weak-Axis End-Plate Joint of the Reinforced Beam to the Column with U-Shaped Connector", Progress in Steel Building Structures, 2023, 25(01): 38-48. (in Chinese)
[18] Nie S.F., Chen S.Y., Wu W.J., Jiang X., Wang S., Lin Y Z. and Liu M X. "An Investigation on the Seismic Behavior of the End-Plate Connection between a Steel Beam and the Weak-Axis of an H-Shaped Column Using a U-Shaped Connector", Buildings, 2024,14(4): 1087.
[19] GB 51022-2015, Technical Code for Steel Structure of Light-Weight Building with Gabled Frames, Ministry of Housing and Urban-Rural Development of the People's Republic of China, Beijing, China, 2015. (in Chinese)
[20] GB 50011-2017, Standard for design of steel structures, Ministry of Housing and Urban-Rural Development of the People's Republic of China, Beijing, China, 2017. (in Chinese)
[21] Baltay, P and Gjelsvik, A. Coefficient of Friction for Steel on Concrete at High Normal Stress[J]. Journal of Material in Civil Engineering,1990,2(1):46-49.
[22] ANSI/AISC 341-10; Seismic Provisons for Structural Steel Buidings. American Institute of Steel Construction: Chicago, IL, USA, 2010.
[23] Goudarzi, A. and Erfani, S. Seismic Performance of Beam to Box-Column Connection by a Short Stub Beam. Journal of Constructional Steel Research, 2022, 190: 107145.
[24] Lou, G.B., Li, G.Q. and Lei, Q., "Recent Developments in the Behavior and Design of High-Strength Bolted End Plate Connections (I)", Progress in Steel Building Structures, 2006, 8, 8–21. (in Chinese)
[25] Lou, G.B., Li, G.Q., Lei, Q., "Recent Developments in the Behavior and Design of High-Strength Bolted End Plate Connections (II)", Progress in Steel Building Structures, 2006, 8, 16–23. (in Chinese)
[26] JGJ 138-2016 Code for Design of Composite Structures, Ministry of Housing and Urban-Rural Development of the People's Republic of China, Beijing, China, 2016. (in Chinese)